Acta Materialia 116 (2016) 354–363

Contents lists available at ScienceDirect

Acta Materialia

journal homepage: www.elsevier.com/locate/actamat

Full length article

A refining mechanism of primary Al_3Ti intermetallic particles by ultrasonic treatment in the liquid state

Feng Wang [a, *], Dmitry Eskin [a, b], Jiawei Mi [c], Thomas Connolley [d], John Lindsay [e], Maher Mounib [f]

[a] Brunel Centre for Advanced Solidification Technology, Brunel University London, Uxbridge, London, UB8 3PH, UK
[b] Tomsk State University, Tomsk, 634050, Russia
[c] School of Engineering, University of Hull, Hull, East Yorkshire HU6 7RX, UK
[d] Diamond Light Source Ltd, Harwell Science & Innovation Campus, Didcot, OX11 0DE, UK
[e] School of Materials, The University of Manchester, Manchester, M13 9PL, UK
[f] Groupe de Physique des Matériaux, UMR CNRS 6634-Université de Rouen, Avenue de l'Université-BP12, 76801 Saint Etienne du Rouvray, France

ARTICLE INFO

Article history:
Received 24 May 2016
Received in revised form
25 June 2016
Accepted 25 June 2016
Available online 6 July 2016

Keywords:
Aluminium alloys
Ultrasonic treatment
Primary intermetallic
Aluminium oxide
Heterogeneous nucleation

ABSTRACT

The mechanism underlying the considerable refinement of primary Al_3Ti intermetallic particles induced by ultrasonic treatment (UST) in an Al-0.4 wt% Ti alloy in the fully liquid state was investigated. Scanning electron microscopy, energy dispersive X-ray spectroscopy, focused ion beam 3D tomography and transmission electron microscopy were used to clearly identify that α-Al_2O_3 particles were located at or near the centres of primary Al_3Ti particles in the samples solidified with and without UST. Crystallographic evaluation using the edge-to-edge matching model and experimental determination of orientation relationships between the α-Al_2O_3 and primary Al_3Ti particles using the convergent beam Kikuchi line diffraction patterns confirmed the high potency of α-Al_2O_3 particles as nucleation sites for the Al_3Ti phase. Based on the experimental results, the refining mechanism is discussed in terms of proposed hypotheses in the literature. It is suggested that the significant refinement of primary Al_3Ti particles upon UST is due to the cavitation-induced deagglomeration and distribution of the α-Al_2O_3 particles and the cavitation-enhanced wetting of the α-Al_2O_3 particles by liquid aluminium.

1. Introduction

The application of high intensity ultrasonic vibrations to the processing of liquid or semi-liquid metals and their alloys is attractive in industrial casting practice because it provides a sustainable and economical method for improving the quality of castings [1,2]. It is well demonstrated that ultrasonic melt treatment (UST) can induce substantial beneficial changes in the microstructure, including the refinement of grains and primary particles, improved structural and chemical homogeneity, and reduced porosity [3]. Among all the effects induced by UST, the refinement of primary intermetallic particles has attracted somewhat less attention in research [2–4]. Under normal conditions, the primary intermetallic particles have a deleterious effect on the ductility and toughness and are harmful to the deformability of as-cast wrought alloys, because they are usually brittle, have elongated shape and may grow to a considerable size, which makes them typical stress concentrators and hence initiators of cracks during casting and deformation processing [5,6]. On the other hand, it is increasingly realised that the primary particles when refined to an appropriate size can act as reinforcement in natural metal-matrix composites [7–10]. In addition, some of the primary intermetallics have shown powerful potential as solidification seeds (grain refiners) for the metal matrices [11–13]. Therefore, significant refinement of the primary particles, especially those that can act as either reinforcing particles or grain refiners, can considerably improve the structure, properties and workability of cast alloys.

A number of mechanisms have been proposed over the years to explain the refinement induced by UST [1,2,11,14,15]. In general, these mechanisms can be grouped as follows [2,11,15,16]: (1) cavitation-enhanced nucleation and (2) cavitation-induced fragmentation. Despite the common recognition of these two main sets, the specific details of the mechanisms are still beyond full

* Corresponding author.
E-mail address: feng.wang@brunel.ac.uk (F. Wang).

http://dx.doi.org/10.1016/j.actamat.2016.06.056

understanding. For example, there is still controversy on the precise mechanism by which cavitation bubbles break the growing solid dendrites or particles [2,15,17]. Is it due to the pulsation of cavitation bubbles, or due to the shock wave arising from the implosive collapse of cavitation bubbles, or both? Several hypotheses have been suggested about the exact mechanism of cavitation-enhanced nucleation of the solid phase. One of those is based on the locally increased undercooling resulting from an increase of the melting point caused by the instantaneous pressure spike as a result of the collapse of cavitation bubbles [18]. Although calculations based on the Clapeyron equation [18] suggest that the increased undercooling may be large enough to promote nucleation, the survival of this first nucleated solid in the superheated melt is under debate. Another mechanism is based on the activation of impurity particles naturally present in the melt, which act as heterogeneous nucleation sites [2,19]. Although quite logical, this hypothesis has up to now received little direct evidence as to what impurity particles act as nucleation sites and how they may be affected by the cavitation bubbles. The observation of oxides or other particles at or near the centre of the intermetallics is typically accepted as evidence of them nucleating these crystals [17,20–23].

Recently, the effect of UST on the refinement of primary Al_3Ti intermetallic particles in an Al-0.4 wt% Ti alloy has been investigated by the authors [24]. High intensity UST was applied at different solidification stages of the primary Al_3Ti phase in an attempt to understand the refining mechanisms of UST. It was found that UST performed from 810 to 770 °C in the fully liquid state of an Al-0.4 wt% Ti alloy, i.e. above the liquidus temperature of the primary Al_3Ti intermetallic, induced significant refinement of primary Al_3Ti particles as shown in Fig. 1. Based on the results of deliberately-designed quenching experiments, it was proposed that the refinement was mainly due to the cavitation-enhanced nucleation of primary Al_3Ti particles via improved wetting of indigenous impurity particles. However, little direct evidence was available at the time to support the hypothesis in this previous paper.

The present work aims at providing specific experimental results to verify the hypothesis made earlier. Therefore, in this current paper, the identity of nucleant particles is first determined and verified by scanning electron microscopy (SEM), energy dispersive X-ray spectroscopy (EDS), focused ion beam (FIB) 3D tomography, and transmission electron microscopy (TEM). Following that, the potency of the nucleant particles as nucleation sites for primary Al_3Ti particles is evaluated from the crystallographic point of view, using the edge-to-edge matching (E2EM) model [25,26]. Furthermore, the orientation relationships between the nucleant particles and primary Al_3Ti particles are experimentally determined by TEM and compared with the predictions of the E2EM model. Finally, the refining mechanism of primary Al_3Ti particles by UST in the fully liquid state is discussed in the light of the above results and the hypotheses proposed in the literature.

2. Experimental

High-purity 99.95% Al (~500 g for each experiment) was melted in a clay-bonded graphite crucible inside an electrical resistance furnace and heated up to 880 ± 3 °C, at which point an Al-10 wt% Ti master alloy was added with mechanical stirring to obtain an Al-0.4 wt% Ti alloy. After 30 min of isothermal holding, the crucible with the melt was transferred to a platform with the ultrasonic equipment (a 5-kW water-cooled magnetostrictive transducer with a conical Nb sonotrode 20 mm in the tip diameter, the sonotrode was pre-heated by immersion in the liquid aluminium in a separate crucible). When the melt temperature decreased to 810 °C, UST was applied by immersing the pre-heated working sonotrode 15 mm below the top melt surface. The working sonotrode was not lifted up from the melt until the melt temperature reached 770 °C. This temperature range was carefully selected to be within the fully

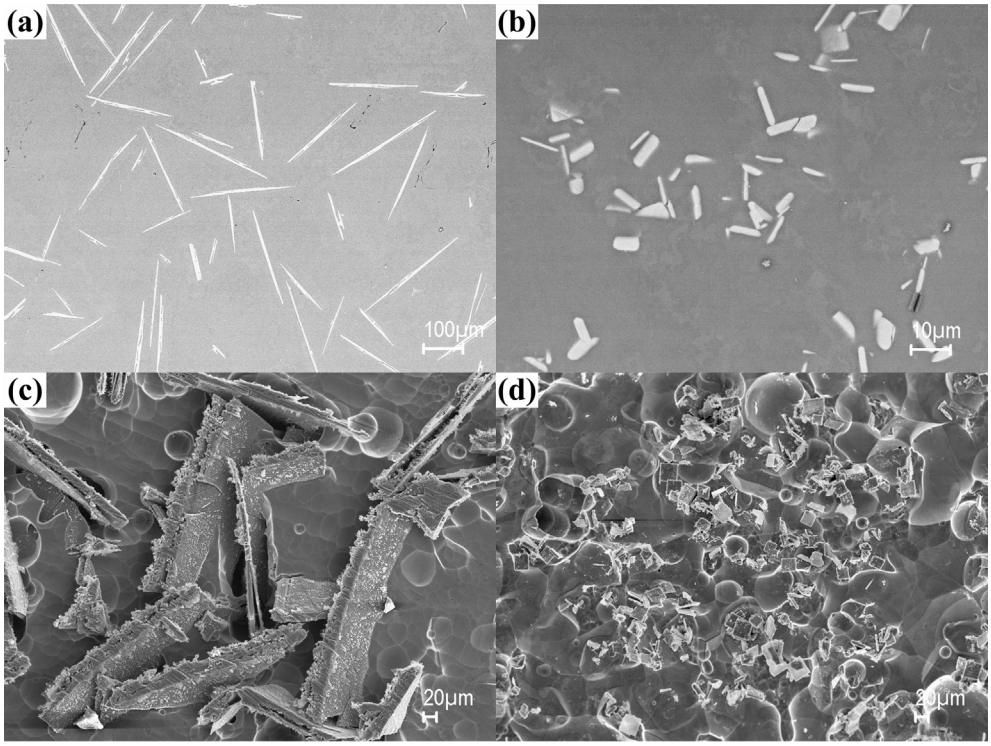

Fig. 1. Typical SEM micrographs of the primary Al_3Ti particles formed in the samples solidified (a) without UST before deep etching; (b) with UST before deep etching; (c) without UST after deep etching; (d) with UST after deep etching. UST performed from 810 to 770 °C.

liquid state as the liquidus temperature of the Al-0.4 wt% Ti alloy is 768 °C. The melt together with the crucible was then left on the platform to solidify and cool in air to room temperature. The overall cooling rate measured by a K-type thermocouple was ~0.8 °C/s. Specimens were cut from the central bottom part of the solidified ingots and then mechanically ground and polished for SEM (ZEISS SUPRA 35VP) observation and EDS mapping. A detailed casting procedure for the ingots and a schematic diagram of specimen position in the ingots can be found elsewhere [24]. A serial FIB technique was used to obtain 3D tomographic data on the relative positions of nucleant and primary Al_3Ti particles. FIB was also used to prepare TEM foils, considering only the particles at/near the centres of primary Al_3Ti particles are potential nucleation sites. First of all, the positions of possible nucleant particles sitting at/near the centre of primary Al_3Ti particles were located by SEM. For the 3D tomography, serial sectioning and imaging was performed as follows: slices of around 65-nm thickness were milled off for a total volume of 25 × 20 × 10 μm^3 and all the cut sections were imaged using the secondary electron detector at 5 kV in a Zeiss NVision 40 SMT FIB-SEM microscope. The 3D reconstruction was performed using Avizo software. For the TEM foil preparation, the possible nucleant particles together with the primary Al_3Ti particles were cut and lifted up by a tungsten manipulator and transferred to an Omni lift-out cooper grid in an FEI Quanta 3D FEG dual beam microscope. After the transfer, the relatively thick foils on the Cu grid were further thinned by the ion beam step by step to around 80 nm. The foils were then examined in a JEOL 2100F TEM operated at 200 kV. The typical serial sectioning for 3D tomography and the milling and lift-up process for TEM foils preparation are illustrated in Fig. 2.

3. Results

3.1. Observation of aluminium oxide particles inside primary Al_3Ti intermetallic particles

During examination in the SEM of the size and morphology of primary Al_3Ti particles in the samples produced with and without UST, unknown particles were spotted at/near the centres of some primary Al_3Ti particles as illustrated in Fig. 3. These unknown particles were considered to be potential nucleation sites for the primary Al_3Ti particles. In order to determine the identity of these particles, EDS mapping was first taken on the areas containing these particles and a typical mapping is shown in Fig. 4. As we can see, the particles were high in O and Al with little Ti, indicating they were probably aluminium oxide particles. In addition, 3D tomography of these areas was also reconstructed to reveal the position of the probable aluminium oxide particles in the primary intermetallics from the 3D point of view. A typical 3D tomography clearly showing a probable aluminium oxide particle inside a primary Al_3Ti particle is displayed in Fig. 5. This further confirmed that the particles are indeed inside the intermetallic, not just attached to the surface, therefore strengthening the hypothesis of them nucleating the intermetallic phase.

3.2. Identification of the crystal structure of aluminium oxide particles

TEM foil samples prepared via the FIB technique were examined and the EDS mappings were first carried out in the TEM to compare with the EDS mapping results obtained by SEM. A typical mapping

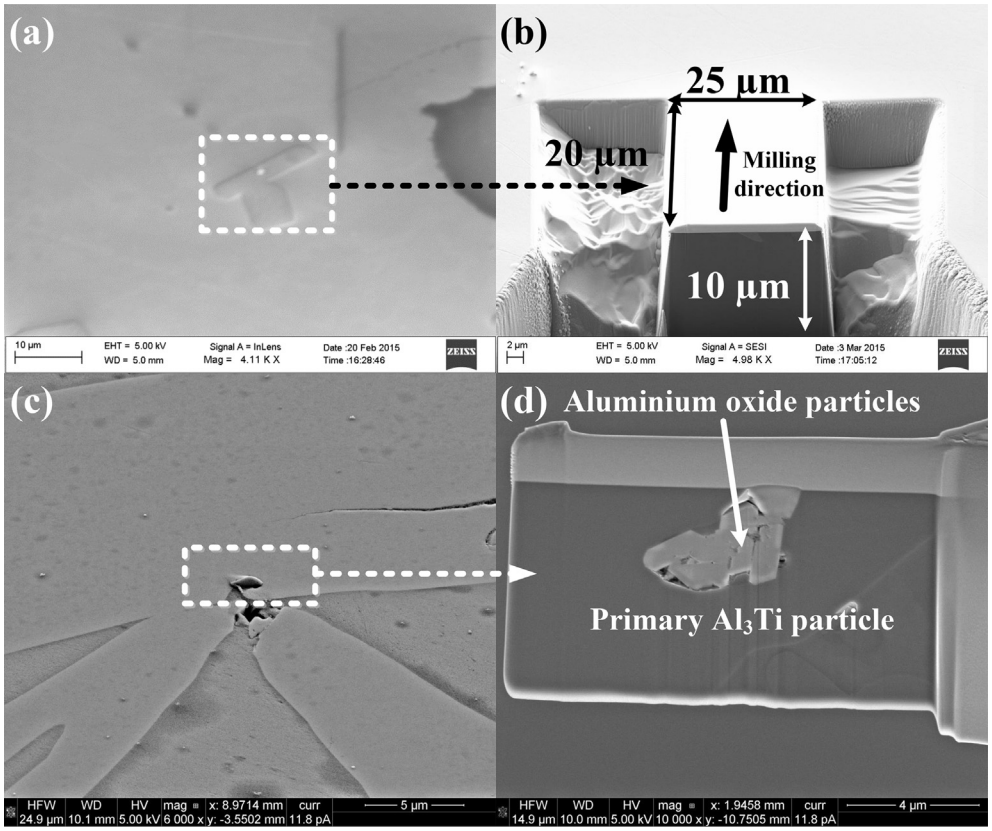

Fig. 2. (a) Typical SEM image of a possible nucleant particle at the centre of an Al_3Ti intermetallic particle after UST; (b) SEM image of (a) after the first sectioning; (c) typical SEM image of a possible nucleant particle near the centre of an Al_3Ti intermetallic particle formed without UST; (d) SEM image of the lift-out sample with the possible nucleant particles embedded in the Al_3Ti intermetallic particle shown in (c).

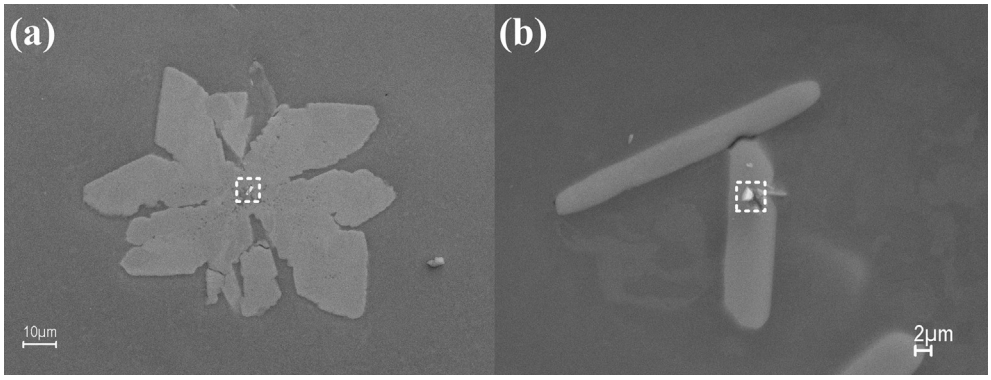

Fig. 3. Typical SEM images of the particles found inside the primary Al_3Ti particles in samples solidified (a) without UST and (b) with UST.

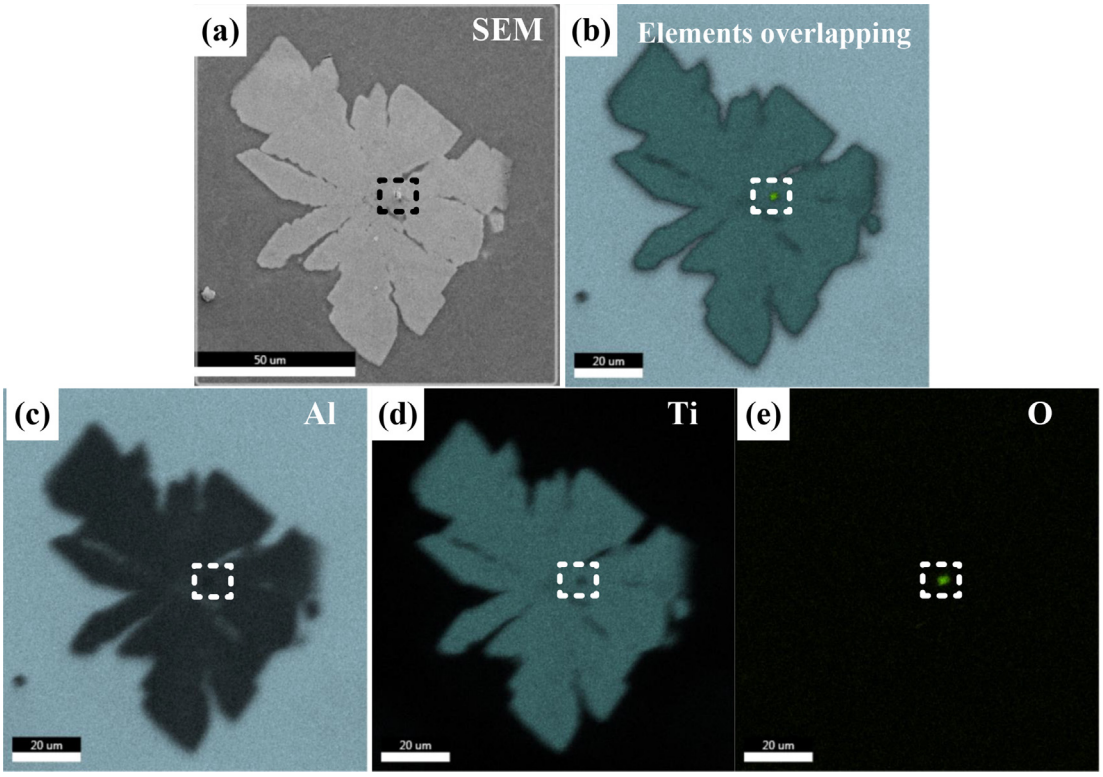

Fig. 4. EDS mapping of a particle inside primary Al_3Ti in a sample solidified without UST: (a) the SEM image; (b) overlapped EDS mapping image of Al, Ti and O elemental distributions; (c) EDS mapping of Al elemental distribution; (d) EDS mapping of Ti elemental distribution; (e) EDS mapping of O elemental distribution.

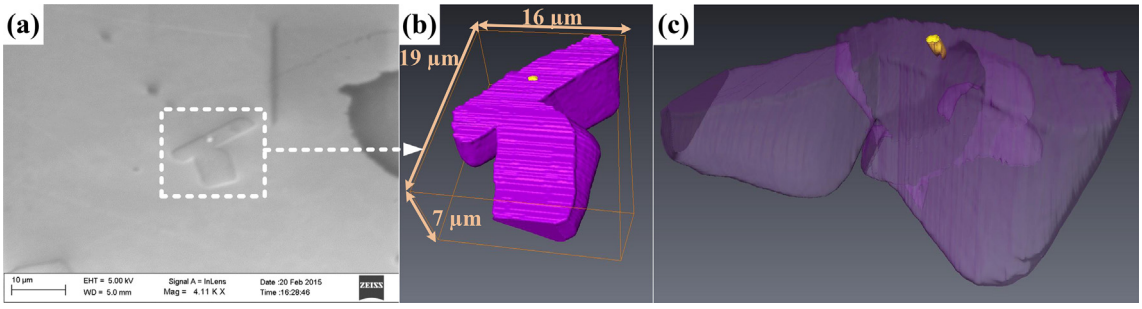

Fig. 5. 3D tomography of a probable aluminium oxide particle (yellow in (b) and (c)) embedded inside a primary Al_3Ti particle (purple) in a sample solidified with UST: (a) SEM image of the analysed area; (b) reconstructed 3D view of the probable aluminium oxide particle and the primary Al_3Ti particle; (c) highlighting the position of the probable aluminium oxide particle by rendering the primary Al_3Ti particles nearly transparent.

of a partial area in the TEM foil sample is shown in Fig. 6. It is clear that the unknown particles contain only Al and O elements without any Ti, which is consistent with the SEM EDS mapping results and hence further corroborates that the unknown particles are aluminium oxide particles.

It is well documented in the literature [27] that aluminium oxide exists in many polymorphs including α-Al_2O_3 (trigonal, $R\bar{3}c$), γ-Al_2O_3 (cubic, $\bar{3}m$), δ-Al_2O_3 (orthorhombic, $P2_12_12_1$), θ-Al_2O_3 (monoclinic, $C2/m$), κ-Al_2O_3 (orthorhombic, $Pna2_1$) and χ-Al_2O_3 (hexagonal, $P6/mm$ or $P6_3/mcm$). Therefore, it was necessary to determine the crystal structure of the aluminium oxide particles observed in the present study.

In order to determine the crystal structure of these aluminium oxide particles, selected area diffraction patterns (SADPs) on each of the aluminium oxide particles after a series of tilting were obtained and indexed. For brevity, the indexed SADPs of a representative aluminium oxide particle after a series of tilting together with the corresponding stereographic Kikuchi map are given in Fig. 7. It was found that all the SADPs obtained on the aluminium oxide particles could be indexed as α-Al_2O_3 and the angles between the indexed beam directions agreed well with the corresponding tilting angles as illustrated in Table 1 and Fig. 7. Combining the SEM and TEM EDS mapping results with the SADPs analysis, it was concluded that the aluminium oxide particles observed at/near the centres of primary Al_3Ti particles are α-Al_2O_3 particles. It is interesting to point out that the aluminium oxide particles normally formed in molten aluminium are reported in the literature [28,29] as γ-Al_2O_3 which has an FCC crystal structure and does not match the SADPs obtained in the present study. It is known that the formation of γ-Al_2O_3 or α-Al_2O_3 particles in molten aluminium depends on many factors such as the alloy chemistry and the melting and casting conditions [28,29]. On heating the metastable γ-Al_2O_3 transforms to the stable α-Al_2O_3 and this transformation is irreversible. The relatively high melting and holding temperature (880 °C) employed in the current melting and casting procedure could be the reason for the formation of α-Al_2O_3 particles (independently or by transformation from γ-Al_2O_3) in the Al-0.4 wt% Ti alloy. Another possibility of the occurrence of α-Al_2O_3 particles could be inheritance from the Al-10 wt% Ti master alloy which was used as the alloying addition.

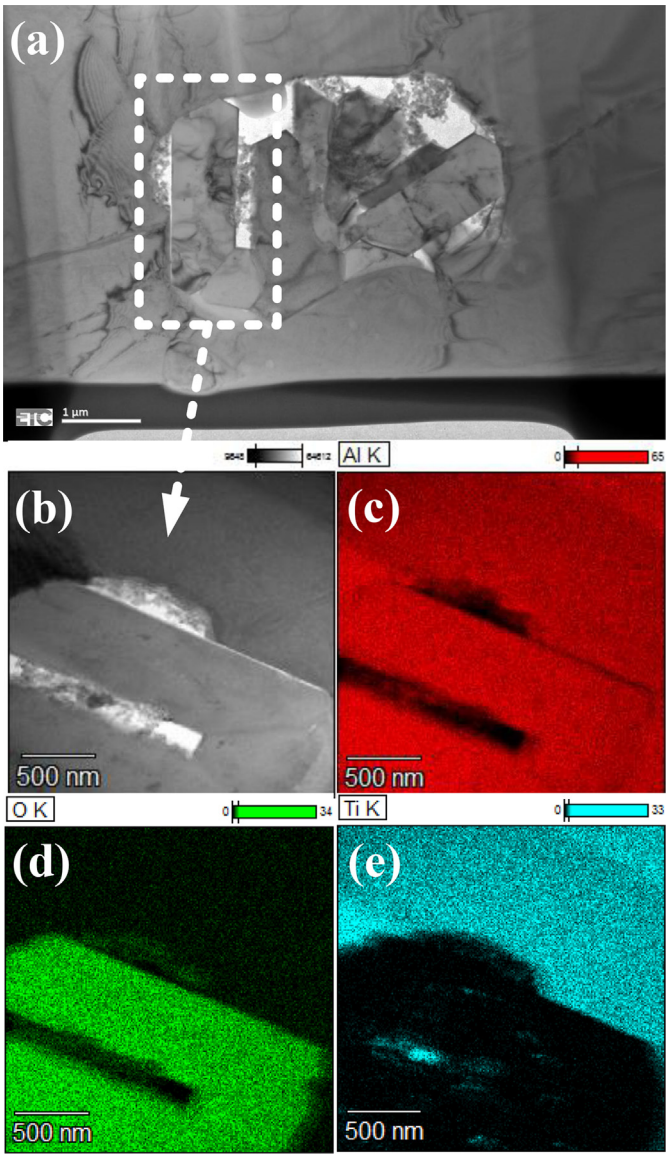

Fig. 6. (a) Overview of a TEM foil sample prepared by FIB from a sample solidified without UST (an agglomerate of several particles found inside Al_3Ti); (b) STEM image of the EDS mapping area; (c) EDS mapping of the Al elemental distribution; (d) EDS mapping of the O elemental distribution; (e) EDS mapping of the Ti elemental distribution.

4. Discussion

4.1. Evaluation of the potency of α-Al_2O_3 as a nucleation site for the primary Al_3Ti phase

Following the identification of α-Al_2O_3 particles, it was important to evaluate the potency of α-Al_2O_3 as a nucleation site for the primary Al_3Ti intermetallic. It is commonly accepted that the interfacial energy between a nucleant particle and the nucleating solid plays a crucial role in determining the potency of the nucleant particle [6,30–32]. A particle that possesses a low-energy interface with the nucleating solid requires only small undercooling to activate heterogeneous nucleation, which means the particle has a strong potency as a nucleation site. In general, the low-energy interface is favourable to good crystallographic matching between the substrate and the newly forming phase [6,30,31]. As a result, the potency of a nucleant particle is usually evaluated by the crystallographic matching between the nucleant particle and the nucleating solid. Typically, the crystallographic matching is determined by the lattice matching [33–35], which is calculated from the lattice parameters only. Although the lattice matching calculation gives reasonable potency evaluation of nucleant particles with simple crystal structures, it lacks accuracy and consistency when the nucleant particles have complex crystal structures. In this case, the atomic matching should be examined rather than the lattice matching as the atoms actually take part in the crystal matching. To facilitate this approach, an edge-to-edge matching (E2EM) model [25,26] that was developed to handle the actual atomic matching was utilised to evaluate the crystallographic matching between the nucleant particle and the nucleating solid. The E2EM model was successfully used to study the potency of common grain refiners in Al and Mg alloys [36–38]. Furthermore, the E2EM model has also achieved success in predicting and developing new inoculants for Mg-Y [39], Mg-Al [40] and Zn [12] alloys.

The fundamentals of the E2EM model have been fully explained elsewhere [36,41] and hence they will not be addressed in detail here. In brief, the crystallographic matching evaluation using the E2EM model involves two major steps: (1) identification of the close-packed (C.P.) atomic rows and C.P. planes based on the crystal structures and atomic positions of both phases and (2) calculation of the interatomic spacing misfit (f_r) along the matching rows and the interplanar spacing mismatch (f_d) between the matching

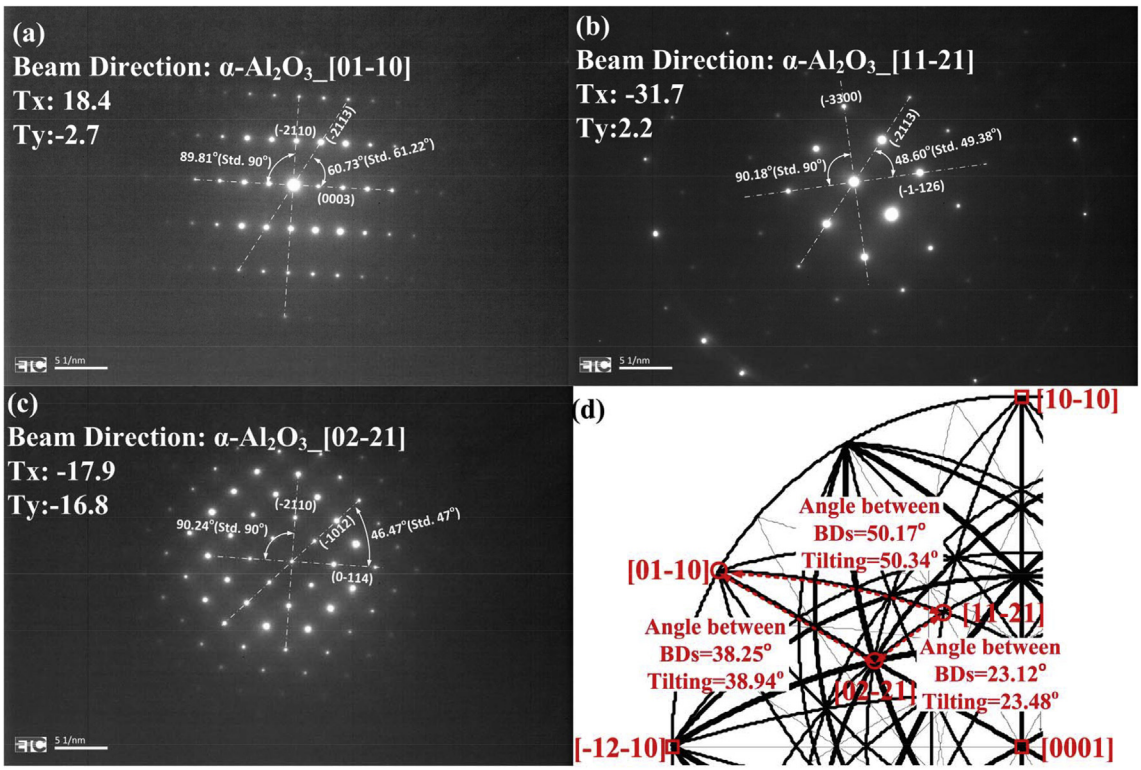

Fig. 7. SADPs obtained from a representative aluminium oxide particle and indexed as α-Al_2O_3 with beam direction (BDs): (a) [01$\bar{1}$ 0]; (b)[11$\bar{2}$ 1]; (c)[02$\bar{2}$ 1]; (d) the corresponding stereographic Kikuchi line map with the angles between BDs and the corresponding tilting angles. Measured values are shown with standard (tabulated) values in parenthesis.

Table 1
Comparison between the values of measured and standard *d*-spacing of planes of α-Al_2O_3.

Plane	*d*-spacing, nm measured	*d*-spacing, nm calculated [30,31]
($\bar{2}$110)	0.2400	0.2375
(0003)	0.4316	0.4323
($\bar{2}$113)	0.2097	0.2082
($\bar{3}$300)	0.1395	0.1371
(1$\bar{1}$26)	0.1595	0.1599
(1$\bar{0}$12)	0.3468	0.3474
(0$\bar{1}$14)	0.2527	0.2547

planes. Al_3Ti has a tetragonal crystal structure with the lattice parameters a = 0.3846 nm and c = 0.8594 nm [42]. Each unit cell contains 6 Al atoms and 2 Ti atoms. The detailed atomic positions can be found in the Refs [42,43]. On the basis of these data, four sets of C.P. planes are identified by the authors: {112}, {200}, {004} and {024} and four sets of C.P. rows are recognised as201^{SS}, 110^{SS}, 421^{ZZ} and 111^{ZZ}. The superscripts "SS" and "ZZ" are used to distinguish the straight and zigzag rows. The α-Al_2O_3 phase has a trigonal crystal structure which can be described by either a rhombohedral or a hexagonal unit cell. In the present study, the hexagonal unit cell is adopted with the lattice parameters a = 0.4759 nm and c = 1.2991 nm [44,45]. It contains 12 Al atoms and 18 O atoms. The precise atomic positions are described in the Refs [44,45]. Therefore, α-Al_2O_3 has four sets of C.P. planes: {11$\bar{2}$3}, {3$\bar{3}$00}, {11$\bar{2}$6}, and {02$\bar{2}$4} and three sets of C.P. rows: 2$\bar{2}$$01^{PS}$, 0$\bar{1}$$11^{PS}$ and 1$\bar{1}$$00^{SS}$. The superscript "PS" indicates that the atomic row is pseudo-straight. Fig. 8 shows the atomic configurations of Al_3Ti and α-Al_2O_3 in their respective most C.P. planes with C.P. rows in these planes highlighted.

Based on the identified C.P. planes and C.P. rows, the interatomic misfit, f_r, and interplanar mismatch, f_d, between Al_3Ti and α-Al_2O_3 were calculated following the formula described in Ref. [46] and the results are illustrated in Fig. 9. According to the E2EM model, the smaller the misfit and mismatch are, the higher the potency of a nucleant is. Furthermore, at least one pair of matching rows with $\boldsymbol{f_r} < 6\%$ and one pair of matching planes that contain the matching rows with $\boldsymbol{f_d} < 10\%$ are required to establish a potential orientation relationship (OR) which is favourable to the formation of coherent or partly coherent interface, i.e. a low-energy interface, between the nucleant particle and the nucleating solid [36,37]. As we can see in Fig. 9(a), there are 4 pairs of matching rows with misfit $\boldsymbol{f_r} < 6\%$ between Al_3Ti and α-Al_2O_3. They are: $1\bar{1}00^{SS}//201^{SS}$, $1\bar{1}00^{SS}//110^{SS}$, $2\bar{2}01^{PS}//421^{ZZ}$, and $0\bar{1}11^{PS}//111^{ZZ}$. There are also two pairs of matching rows with $\boldsymbol{f_r}$ slightly larger than 6%: $0\bar{1}11^{PS}//110^{SS}$ = 6.28% and $0\bar{1}11^{PS}//421^{ZZ}$ = 6.13%. In the present study, they are also included for evaluation and prediction since the critical value of 6% misfit is an empirical estimation based on a large number of common grain refiners and experimentally observed ORs [36,37]. Fig. 9(b) also shows that 5 pairs of matching planes between Al_3Ti and α-Al_2O_3 have the mismatch $\boldsymbol{f_d} < 10\%$. These are: {11$\bar{2}$3}//{112}, {11$\bar{2}$3}//{200}, {11$\bar{2}$3}//{004}, {3$\bar{3}$00}//{024}, and {11$\bar{2}$6}//{024}.

Combining the matching row pairs with the associated matching plane pairs that contain the matching rows, 6 possible ORs are obtained as listed in Table 2.

These possible ORs can be further refined using the $\boldsymbol{\Delta \vec{g}}$ criterion [47,48], where $\boldsymbol{\Delta \vec{g}}$ is a displacement vector of the two $\vec{g}$ s in reciprocal space for the two sets of planes that form an intersection plane. After the refinement, three distinguishable ORs are finally predicted as listed in Table 3. From the above calculation of misfit and mismatch (Fig. 9) and prediction of potential ORs (Table 3), it is clear that α-Al_2O_3 has good crystallographic matching with Al_3Ti,

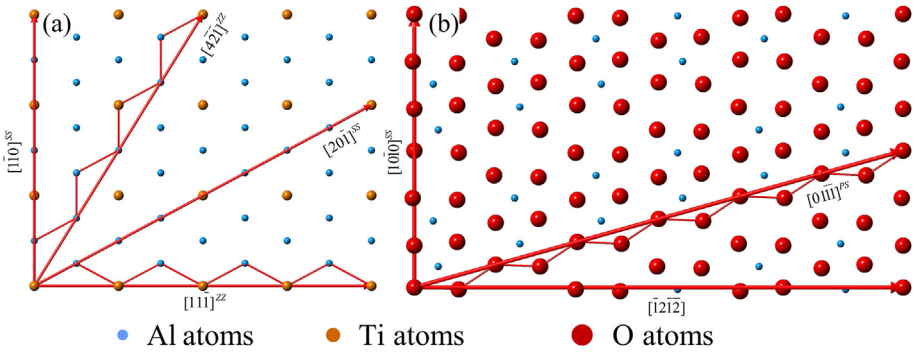

Fig. 8. Atomic configuration ions of Al_3 Ti and α $-Al_2$ O_3 in their most close - packed planes: (a) $(112)_{A13Ti}$; (b) $(1\bar{2}\ 1\bar{3})_{\alpha\text{-}Al2O3}$.

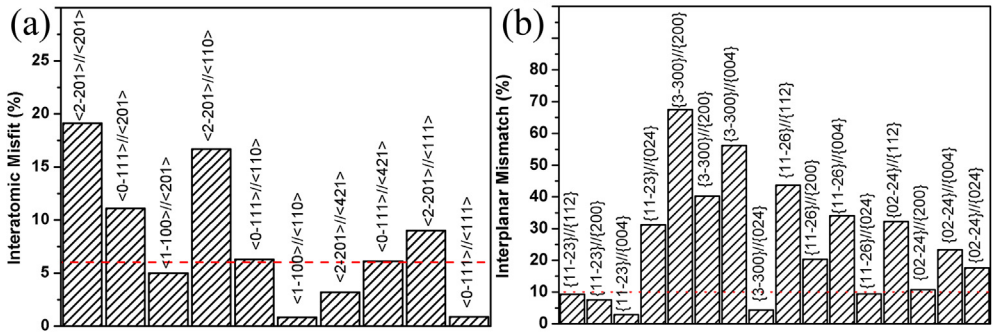

Fig. 9. The calculated values of (a) interatomic spacing misfit, f_i, between Al_3Ti and α-Al_2O_3, and (b) interplanar spacing mismatch, f_d, between Al_3Ti and α-Al_2O_3.

Table 2
Possible crystallographic ORs between Al_3Ti and α-Al_2O_3.

ORs	Parallel direction	Parallel plane
OR(1)	$1\bar{1}00^{SS}_{Al_2O_3}//110^{SS}_{Al_3Ti}$	$\{11\bar{2}3\}_{Al_2O_3}//\{004\}_{Al_3Ti}$
OR(2)	$0\bar{1}11^{PS}_{Al_2O_3}//111^{ZZ}_{Al_3Ti}$	$\{11\bar{2}3\}_{Al_2O_3}//\{112\}_{Al_3Ti}$
OR(3)	$2\bar{2}01^{PS}_{Al_2O_3}//421^{ZZ}_{Al_3Ti}$	$\{11\bar{2}6\}_{Al_2O_3}//\{024\}_{Al_3Ti}$
OR(4)	$1\bar{1}00^{SS}_{Al_2O_3}//201^{SS}_{Al_3Ti}$	$\{11\bar{2}3\}_{Al_2O_3}//\{112\}_{Al_3Ti}$
OR(5)	$0\bar{1}11^{PS}_{Al_2O_3}//421^{ZZ}_{Al_3Ti}$	$\{11\bar{2}3\}_{Al_2O_3}//\{112\}_{Al_3Ti}$
OR(6)	$0\bar{1}11^{PS}_{Al_2O_3}//110^{SS}_{Al_3Ti}$	$\{11\bar{2}3\}_{Al_2O_3}//\{004\}_{Al_3Ti}$

the α-Al_2O_3 particles embedded in an Al_3Ti particle and the corresponding convergent-beam Kikuchi line diffraction patterns. After indexing the patterns, the OR shown in Fig. 10 can be expressed as follows:

$[\bar{1}100]_{\alpha-Al_2O_3}$ 1.02° from $[110]_{Al_3Ti}$, $(11\bar{2}3)_{\alpha-Al_2O_3}$ 3.27° from $(00\bar{4})_{Al_3Ti}$, $(11\bar{2}3)_{\alpha-Al_2O_3}$ 1.92° from $(1\bar{1}2)_{Al_3Ti}$.

It is obvious that the experimentally determined OR agrees well with the OR (A) in Table 3 predicted by E2EM model. The consistency between the experimental and predicted ORs substantiates the evaluation by E2EM model.

Table 3
Final crystallographic ORs between Al_3Ti and α-Al_2O_3 predicted using the E2EM model and the $\Delta\vec{g}$ criterion.

ORs	Parallel direction	Parallel or nearly parallel plane (1)	Parallel or nearly parallel plane (2)
OR(A)	$[\bar{1}100]^{SS}_{Al_2O_3}//[110]^{SS}_{Al_3Ti}$	$(11\bar{2}3)_{Al_2O_3}$ 1.92° from $(00\bar{4})_{Al_3Ti}$	$(11\bar{2}3)_{Al_2O_3}$ 1.45° from $(1\bar{1}2)_{Al_3Ti}$
OR(B)	$[\bar{1}100]^{SS}_{Al_2O_3}//[02\bar{1}]^{SS}_{Al_3Ti}$	$(11\bar{2}3)_{Al_2O_3}$ 0.76° from $(1\bar{1}2)_{Al_3Ti}$	$(11\bar{2}3)_{Al_2O_3}$ 4.99° from $(200)_{Al_3Ti}$
OR(C)	$[0\bar{1}11]^{PS}_{Al_2O_3}//[110]^{SS}_{Al_3Ti}$	$(1\bar{2}1\bar{3})_{Al_2O_3}$ 0.34° from $(00\bar{4})_{Al_3Ti}$	$(\bar{2}110)_{Al_2O_3}$ 6.08° from $(1\bar{1}2)_{Al_3Ti}$

implying that α-Al_2O_3 particles can be potent nucleant particles for primary Al_3Ti particles from the crystallographic point of view.

4.2. Experimental verification of ORs predicted by the E2EM model

In order to verify the evaluation and prediction of the E2EM model, the ORs between Al_3Ti and α-Al_2O_3 were experimentally determined using the convergent-beam Kikuchi line diffraction pattern from the FIB TEM foil samples. Four FIB samples were examined: two were prepared from the alloys solidified after UST and the other two were from the alloys without UST. A distinguishable OR was determined. Fig. 10 shows a typical TEM image of

4.3. Refining mechanism of primary Al_3Ti particles by UST in the fully liquid state

Both the theoretical evaluation by E2EM model and the experimental examination by TEM confirmed that the α-Al_2O_3 particles can act as heterogeneous nucleation sites for primary Al_3Ti particles in the alloys produced with and without UST. It is also widely recognised [1,2,14,15,49] that the effects of UST essentially arise from the two most important phenomena that occur during the propagation of high intensity ultrasound waves in the liquid: (i) acoustic cavitation which is the formation, growth and implosive collapse of cavitation bubbles and (ii) acoustic streaming which is

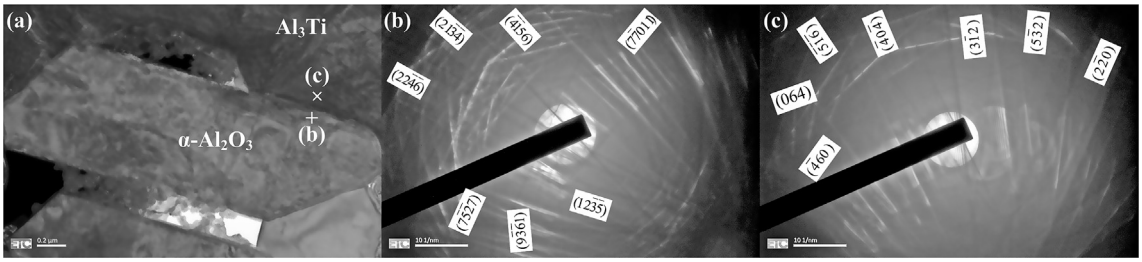

Fig. 10. (a) Typical bright-field TEM image showing the α-Al_2O_3 particles embedded in an Al_3Ti particle; (b) Kikuchi pattern from the α-Al_2O_3 particle; (c) Kikuchi pattern from the Al_3Ti particle.

the formation of a steady circulation flow driven by acoustic wave propagation and cavitation region pulsation. In the light of these, the observed refining effect induced by UST in the fully liquid state on the primary Al_3Ti (see Fig. 1) can be attributed to the combined effect of (1) the cavitation-enhanced wetting of the α-Al_2O_3 particles by Al alloy melt and (2) the cavitation-induced deagglomeration and acoustic streaming-aided distribution of the α-Al_2O_3 particles.

It is important to note that gas (hydrogen in liquid aluminium) tends to absorb at the surface of oxide particles [29]. The presence of a gaseous phase at the surface of oxide particles hinders the access of the liquid to the particles thus preventing the wetting by the melt. As a consequence, the majority of the α-Al_2O_3 particles remain inert with respect to the melt and do not act as potent nucleants during solidification under normal conditions. However, with the application of UST, the formation, growth and collapse of cavitation bubbles literally strip the α-Al_2O_3 particles of the absorbed gas and make them accessible by the surrounding melt, thus enhancing the wetting [2]. This cavitation-enhanced wetting of α-Al_2O_3 particles makes more particles available as substrates for heterogeneous nucleation and therefore facilitates the refinement of primary Al_3Ti particles.

It is well known that the cavitation bubbles preferentially form at the weak points in the liquid such as solid impurity particles and gas pockets [1,2]. Therefore, the agglomerates of particles or the particles themselves are ideal nucleation sites for cavitation bubbles. In such a case, the cavitation bubbles first nucleate, then pulsate and eventually collapse at the interface of α-Al_2O_3 particles when the UST is applied in the fully liquid state. The intensive pulsation gradually loosens the agglomerates of α-Al_2O_3 particles

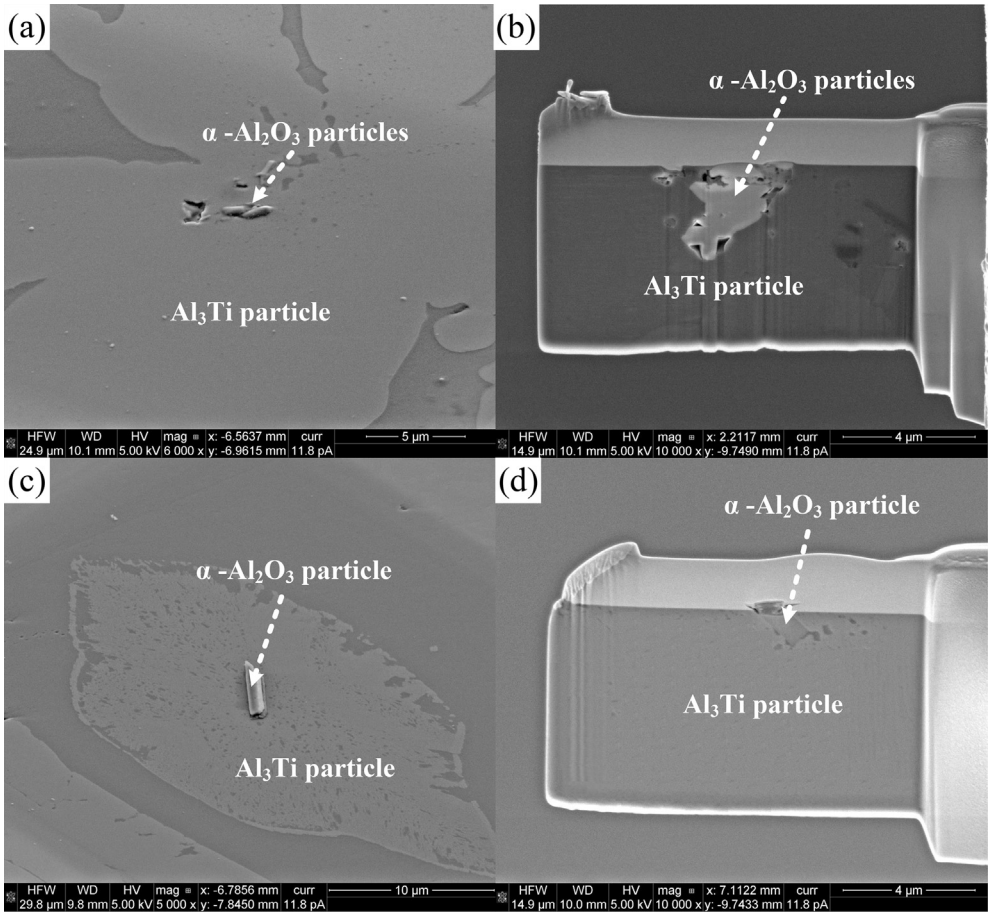

Fig. 11. SEM images of TEM foil samples prepared by FIB: (a) and (b) sample prepared from the alloy without UST, showing a cluster of α-Al_2O_3 particles in a single primary Al_3Ti particle; (c) and (d) sample prepared from the alloy subjected to UST, showing only one α-Al_2O_3 particle in a single primary Al_3Ti particle.

and the final implosive collapse that produces high pressure shock waves and cumulative jets can be strong enough to separate particles from the agglomerates. Following that, the acoustic streaming then distributes these dispersed α-Al_2O_3 particles throughout the whole volume of the melt, which significantly increases the number of the α-Al_2O_3 particles available as substrates for heterogeneous nucleation and hence further promotes the refinement of primary Al_3Ti particles. A similar mechanism of deagglomeration and dispersion was suggested for composite materials produced with ultrasonic processing [7,50,51]. During the preparation of TEM foil samples using FIB, it was noticed that, for the samples prepared from the alloys without UST, there was more than one α-Al_2O_3 particle forming a cluster inside a single primary Al_3Ti particle even though only one α-Al_2O_3 particle could be observed on the polished surface in the SEM as shown in Fig. 2(c) and (d). In comparison, there was only a single α-Al_2O_3 particle inside the primary Al_3Ti particle in the samples prepared from the alloys subjected to UST as presented in Fig. 5. This difference was also observed in the other two samples (one without UST and one with UST) as shown in Fig. 11. This consistent (if not statistical) observation of different numbers of α-Al_2O_3 particles inside a single primary Al_3Ti particle could be partial evidence for the cavitation-induced deagglomeration effect.

In summary, on one hand, α-Al_2O_3 particles or agglomerates of α-Al_2O_3 particles are favourable sites for the development of cavitation bubbles. On the other hand, the pulsation and collapse of cavitation bubbles break up the agglomerates of α-Al_2O_3 particles, remove the absorbed gas from their surface, and distribute α-Al_2O_3 particles throughout the melt. All these effects work in concert to promote the heterogeneous nucleation, multiplying the nucleation sites and hence resulting in the refinement of primary Al_3Ti particles.

5. Conclusions

The current paper presents a study on the refining mechanism of primary Al_3Ti particles in an Al-0.4 wt% Ti alloy induced by UST in the fully liquid state. The obtained results and analysis allow us to draw the following conclusions:

1. α-Al_2O_3 particles are identified at or near the centres of primary Al_3Ti particles by SEM and TEM in combination with EDS and SADPs analysis.
2. The evaluation by E2EM model and the ORs determination by TEM confirm that the α-Al_2O_3 particles are potent nucleants for the primary Al_3Ti particles.
3. The significant refinement of primary Al_3Ti particles by ultrasonic treatment performed in the fully liquid state observed in the current study is attributed to (i) the cavitation-induced deagglomeration and distribution of α-Al_2O_3 particles and (ii) the cavitation-enhanced wetting of α-Al_2O_3 particles by aluminium melt. Both effects work together to facilitate the heterogeneous nucleation and hence lead to the refinement of primary Al_3Ti particles.

Acknowledgements

The authors acknowledge the financial support from UK government's Engineering and Physical Science Research Council (EPSRC) for the Ultra-Cast project [Grant EP/L019884/1, EP/L019825/1, and EP/L019965/1]. The authors are also very grateful to Professor Grace Burke at The University of Manchester and Professor Williams Lefebvre at University De Rouen for their help with the FIB experiments. Dr Dong Qiu at RMIT University is also acknowledged for his critical comments and constructive suggestions on the manuscript.

References

[1] O.V. Abramov, High-intensity Ultrasonics: Theory and Industrial Applications, Gordon and Breach Science Publishers, Amsterdam, The Netherlands, 1998.
[2] G.I. Eskin, D.G. Eskin, Ultrasonic Treatment of Light Alloy Melts, CRC Press, Boca Raton, Florida, 2015.
[3] G.I. Eskin, Broad prospects for commercial application of the ultrasonic (cavitation) melt treatment of light alloys, Ultrason. Sonochem. 8 (2001) 319–325.
[4] L. Zhang, D.G. Eskin, L. Katgerman, Influence of ultrasonic melt treatment on the formation of primary intermetallics and related grain refinement in aluminum alloys, J. Mater. Sci. 46 (2011) 5252–5259.
[5] J.A. Dantzig, M. Rappaz, Solidification, EPFL Press, Lausanne, 2009.
[6] W. Kurz, D.J. Fisher, Fundamentals of Solidification, Trans Tech Publications, Switzerland, 1998.
[7] G.I. Eskin, D.G. Eskin, Production of natural and synthesized aluminum-based composite materials with the aid of ultrasonic (cavitation) treatment of the melt, Ultrason. Sonochem. 10 (2003) 297–301.
[8] R.A. Varin, Intermetallic-reinforced light-metal matrix in-situ composites, Metall. Mater. Trans. A 33 (2002) 193–201.
[9] R.A. Varin, Intermetallic-reinforced Al and Al-Mg matrix in-situ composites, Process. Fabr. Adv. Mater. X (2001) 301–318.
[10] S.C. Tjong, Z.Y. Ma, Microstructural and mechanical characteristics of in situ metal matrix composites, Mater. Sci. Eng. R Rep. 29 (2000) 49–113.
[11] T.V. Atamanenko, D.G. Eskin, L. Zhang, L. Katgerman, Criteria of grain refinement induced by ultrasonic melt treatment of aluminum alloys containing ZR and Ti, Metall. Mater. Trans. A 41 (2010) 2056–2066.
[12] Z. Liu, D. Qiu, F. Wang, J.A. Taylor, M. Zhang, The grain refining mechanism of cast zinc through silver inoculation, Acta Mater 79 (2014) 315–326.
[13] F. Wang, Z. Liu, D. Qiu, J.A. Taylor, M.A. Easton, M.X. Zhang, Revisiting the role of peritectics in grain refinement of Al alloys, Acta Mater 61 (2013) 360–370.
[14] M. Qian, A. Ramirez, A. Das, Ultrasonic refinement of magnesium by cavitation: clarifying the role of wall crystals, J. Cryst. Growth 311 (2009) 3708–3715.
[15] J.R.G. Sander, B.W. Zeiger, K.S. Suslick, Sonocrystallization and sonofragmentation, Ultrason. Sonochem. 21 (2014) 1908–1915.
[16] A. Ramirez, M. Qian, B. Davis, T. Wilks, High-intensity ultrasonic grain refinement of magnesium alloys: role of solute, Int. J. Cast. Metals Res. 22 (2009) 260–263.
[17] T.V. Atamanenko, D.G. Eskin, M. Sluiter, L. Katgerman, On the mechanism of grain refinement in Al–Zr–Ti alloys, J. Alloys Compd. 509 (2011) 57–60.
[18] J.D. Hunt, K.A. Jackson, Nucleation of solid in an undercooled liquid by cavitation, J. Appl. Phys. 37 (1966) 254–257.
[19] Y. Han, K. Li, J. Wang, D. Shu, B. Sun, Influence of high-intensity ultrasound on grain refining performance of Al-5Ti-1B master alloy on aluminium, Mater. Sci. Eng. A 405 (2005) 306–312.
[20] L. Zhang, D.G. Eskin, A.G. Miroux, L. Katgerman, On the mechanism of the formation of primary intermetallics under ultrasonic melt treatment in an Al-Zr-Ti alloy, IOP Conf. Ser. Mater. Sci. Eng. 27 (2012) 012002.
[21] Z. Fan, Y. Wang, Z.F. Zhang, M. Xia, H.T. Li, J. Xu, L. Granasy, G.M. Scamans, Shear enhanced heterogeneous nucleation in some Mg- and Al-alloys, Int. J. Cast. Metals Res. 22 (2009) 318–322.
[22] K.B. Hyde, A.F. Norman, P.B. Prangnell, The effect of cooling rate on the morphology of primary Al3Sc intermetallic particles in Al-Sc alloys, Acta Mater 49 (2001) 1327–1337.
[23] D.N. Miller, L. Lu, A.K. Dahle, The role of oxides in the formation of primary iron intermetallics in an Al-11.6Si-0.37Mg alloy, Metall. Mater. Trans. B 37 (2006) 873–878.
[24] F. Wang, D. Eskin, T. Connolley, J. Mi, Effect of ultrasonic melt treatment on the refinement of primary Al3Ti intermetallic in an Al–0.4Ti alloy, J. Cryst. Growth 435 (2016) 24–30.
[25] M.X. Zhang, P.M. Kelly, Edge-to-edge matching and its applications: part I. Application to the simple HCP/BCC system, Acta Mater 53 (2005) 1073–1084.
[26] M.X. Zhang, P.M. Kelly, Edge-to-edge matching and its applications: part II. Application to Mg–Al, Mg–Y and Mg–Mn alloys, Acta Mater 53 (2005) 1085–1096.
[27] I. Levin, D. Brandon, Metastable alumina polymorphs: crystal structures and transition sequences, J. Am. Ceram. Soc. 81 (1998) 1995–2012.
[28] Y. Wang, H.T. Li, Z. Fan, Oxidation of aluminium alloy melts and inoculation by oxide particles, Trans. Indian Inst. Metals 65 (2012) 653–661.
[29] V.I. Dobatkin, R.M. Gabidullin, B.A. Kolachev, G.S. Makarov, Gases and oxides in aluminum wrought alloys, Metallurgiya 39 (1976) 103–113.
[30] D.A. Porter, K.E. Easterling, M.Y. Sherif, Phase Transformations in Metals and Alloys, CRC Press, Boca Raton, FL, 2009.
[31] J.W. Christian, Chapter 14-Solidification and Melting. The Theory of Transformations in Metals and Alloys, Oxford, Pergamon, 2002, pp. 623–701.
[32] P.D. Dankov, Crystallochemical mechanism of interaction between the crystal surface and foreign elemental particles, Zh. Fiz. Khim. Russ. J. Phys. Chem. 20 (1946) 15.
[33] B.L. Bramfitt, The effect of carbide and nitride additions on the heterogeneous nucleation behavior of liquid iron, Metall. Trans. 1 (1987-1995).
[34] M. Johnsson, L. Eriksson, Thermal expansion of Al and TiB2 in the temperature range 300 to 900 K and calculated lattice fit at the melting temperature for Al, Z. Met. 89 (1998) 478–480.

[35] G.P. Jones, J. Pearson, Factors affecting grain refinement of aluminum using titanium and boron additives, Metall. Trans. B Process Metall. 7 (1976) 223–234.
[36] M.X. Zhang, P.M. Kelly, M.A. Easton, J.A. Taylor, Crystallographic study of grain refinement in aluminum alloys using the edge-to-edge matching model, Acta Mater 53 (2005) 1427–1438.
[37] M.X. Zhang, P.M. Kelly, M. Qian, J.A. Taylor, Crystallography of grain refinement in Mg–Al based alloys, Acta Mater 53 (2005) 3261–3270.
[38] D. Qiu, M.X. Zhang, H.M. Fu, P.M. Kelly, J.A. Taylor, Crystallography of recently developed grain refiners for Mg–Al alloys, Philos. Mag. Lett. 87 (2007) 505–514.
[39] D. Qiu, M.X. Zhang, J.A. Taylor, P.M. Kelly, A new approach to designing a grain refiner for Mg casting alloys and its use in Mg-Y-based alloys, Acta Mater 57 (2009) 3052–3059.
[40] H.M. Fu, M.X. Zhang, D. Qiu, P.M. Kelly, J.A. Taylor, Grain refinement by AlN particles in Mg-Al based alloys, J. Alloys Compd. 478 (2009) 809–812.
[41] M.X. Zhang, P.M. Kelly, M.A. Easton, J.A. Taylor, Crystallographic study of grain refinement in aluminum alloys using the edge-to-edge matching model, Acta Mater 53 (2005) 1427–1438.
[42] J.L.C. Daams, P. Villars, J.H.N.v. Vucht, Atlas of Crystal Structure Types for Intermetallic Phases, ASM International, Materials Park, Ohio, 1991.
[43] P. Villars, L.D. Calvert, Pearson's Handbook of Crystallographic Data for Intermetallic Phases, ASM International, Materials Park, Ohio, 1991.
[44] M.L. Kronberg, Plastic deformation of single crystals of sapphire: basal slip and twinning, Acta Metall. 5 (1957) 507–524.
[45] W.E. Lee, K.P.D. Lagerlof, Structural and electron diffraction data for sapphire (alpha-Al_2O_3), J. Electron Microsc. Tech. 2 (1985) 247–258.
[46] D. Qiu, J.A. Taylor, M.X. Zhang, Understanding the Co-poisoning effect of Zr and Ti on the grain refinement of cast aluminum alloys, Metall. Mater. Trans. A Phys. Metall. Mater. Sci. 41 (2010) 3412–3421.
[47] W.Z. Zhang, G.R. Purdy, O-lattice analyses of interfacial misfit. 1. General considerations, Philos. Mag. a Phy. Condens. Matter Struct. Defects Mech. Prop. 68 (1993) 279–290.
[48] W.Z. Zhang, G.R. Purdy, O-lattice analyses of interfacial misfit. 2. Systems containing invariant lines, Philos. Mag. a- Phy. Condens. Matter Struct. Defects Mech. Prop. 68 (1993) 291–303.
[49] M. Qian, A. Ramirez, A. Das, D.H. Stjohn, The effect of solute on ultrasonic grain refinement of magnesium alloys, J. Cryst. Growth 312 (2010) 2267–2272.
[50] L. Ma, F. Chen, G. Shu, Preparation of fine particulate reinforced metal matrix composites by high intensity ultrasonic treatment, J. Mater. Sci. Lett. 14 (1995) 649–650.
[51] Y. Yang, J. Lan, X. Li, Study on bulk aluminum matrix nano-composite fabricated by ultrasonic dispersion of nano-sized SiC particles in molten aluminum alloy, Mater. Sci. Eng. A 380 (2004) 378–383.